

# Towards Effective and Efficient Context-aware Nucleus Detection in Histopathology Whole Slide Images

Zhongyi Shui<sup>1,2</sup>, Ruizhe Guo<sup>1,2</sup>, Honglin Li<sup>1,2</sup>, Yuxuan Sun<sup>1,2</sup>, Yunlong Zhang<sup>1,2</sup>, Chenglu Zhu<sup>2</sup>, Jiatong Cai<sup>2</sup>, Pingyi Chen<sup>1,2</sup>, Yanzhou Su<sup>3</sup>, and Lin Yang<sup>2,4\*</sup>

<sup>1</sup> College of Computer Science and Technology, Zhejiang University

<sup>2</sup> School of Engineering, Westlake University

<sup>3</sup> DAMO Academy, Alibaba Group

<sup>4</sup> Center for Interdisciplinary Research and Innovation, Muyuan Lab

**Abstract.** Nucleus detection in histopathology whole slide images (WSIs) is crucial for a broad spectrum of clinical applications. Current approaches for nucleus detection in gigapixel WSIs utilize a sliding window methodology, which overlooks boarder contextual information (*e.g.*, tissue structure) and easily leads to inaccurate predictions. To address this problem, recent studies additionally crops a large Filed-of-View (FoV) region around each sliding window to extract contextual features. However, such methods substantially increases the inference latency. In this paper, we propose an effective and efficient context-aware nucleus detection algorithm. Specifically, instead of leveraging large FoV regions, we aggregate contextual clues from off-the-shelf features of historically visited sliding windows. This design greatly reduces computational overhead. Moreover, compared to large FoV regions at a low magnification, the sliding window patches have higher magnification and provide finer-grained tissue details, thereby enhancing the detection accuracy. To further improve the efficiency, we propose a grid pooling technique to compress dense feature maps of each patch into a few contextual tokens. Finally, we craft OCELOT-seg, the first benchmark dedicated to context-aware nucleus instance segmentation. Code, dataset, and model checkpoints will be available at <https://github.com/windygoo/PathContext>.

**Keywords:** Computational pathology · Nucleus detection.

## 1 Introduction

Nucleus detection in histopathology whole slide images (WSIs) is a fundamental task in computational pathology. It allows quantitative analysis of WSIs, which can lead to better cancer diagnosis, grading, prognosis, and treatment planning while maintaining medical interpretability [6,20]. Therefore, the development of

---

\* Corresponding author

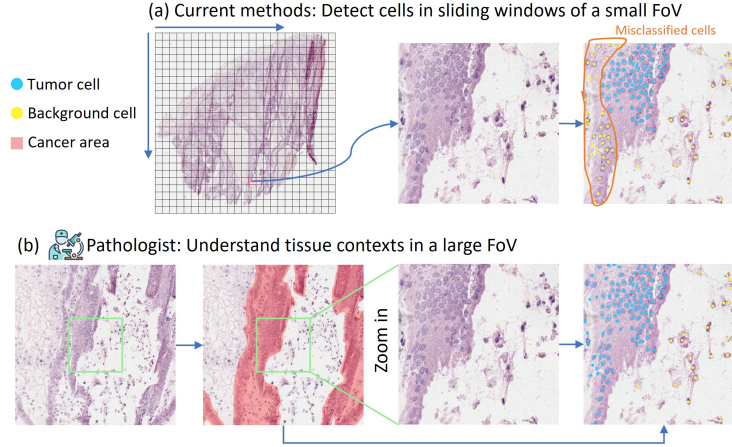


Fig. 1: (a) Typical nucleus detection methods operate on gigapixel WSIs in a sliding window manner. The model detects nuclei in each window patch without understanding boarder tissue structure, which easily leads to inaccurate predictions. (b) Pathologists first zoom out to examine the tissue context at large FoVs and then zoom in to observe detailed nuclear morphology for accurate assessments [20].

precise automatic nucleus detection algorithms has become a critical research focus in recent years. Current nucleus detection pipeline involves training a nucleus detector using expert-annotated histopathology patches and then deploys it to detect nuclei in gigapixel WSIs through a sliding window technique [14,21,27,13], as illustrated in Fig. 1 (a). However, for accurate nucleus localization, the annotated and sliding window patches are cropped at high magnification but small Field-of-View (FoV) [20]. As a result, the nucleus detector can only see a limited context without understanding boarder tissue information, which can easily lead to inaccurate predictions. In clinical practice, pathologists first examine the tissue context at large FoVs and then zoom in to observe detailed nuclear morphology for accurate assessments (see Fig. 1 (b)).

Inspired by this clinical workflow, recent works [1,2,23,20] utilize a large FoV patch, which has the same resolution as sliding window patches but encompass boarder WSI regions, as a supplementary input of nucleus detectors to enable context-aware nucleus detection. Specifically, as shown in Fig. 2 (b), they integrate the context-enriched features from the large FoV patch into the hidden embeddings of the small FoV patch through feature cropping and fusion techniques. Despite the improved outcomes, we argue that this line of approaches exhibits two critical limitations: (1) Due to the substantial difference in data distribution (*i.e.*, magnification levels), these studies utilize separate image encoders to process patches at different FoVs, which greatly increases the computational overhead. (2) The requirement for additional processing the large FoV patches,

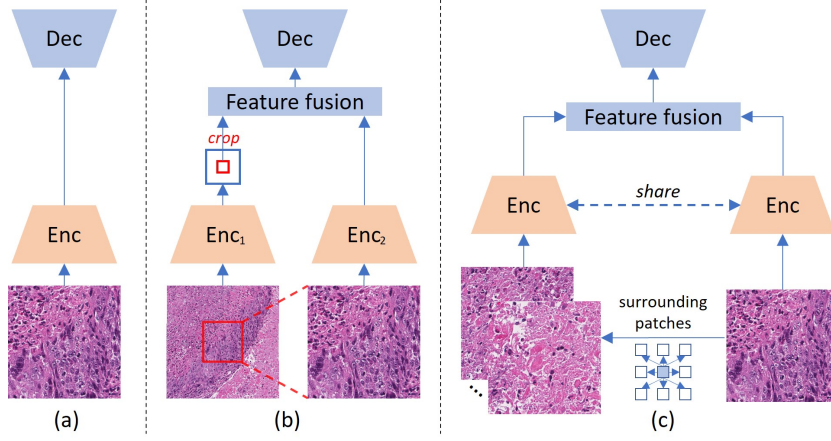


Fig. 2: Pipeline comparison. (a) Typical nucleus detectors operate on patches of a single FoV without considering tissue context. (b) Previous context-aware nucleus detection approaches leverage a large FoV patch to extract contextual information. (c) Our method aggregates contextual information from off-the-shelf features of historically visited surrounding patches during whole-slide inference.

including data preparation and feature extraction, significantly increases the inference time.

In this work, we propose to aggregate contextual information from patches that surround with the region-of-interest (ROI) patch, as illustrated by Fig. 2 (c). Notably, in the training stage, the ROI patch comes from the annotated set while during inference on WSIs, the ROI patch and its surrounding patches are both part of sliding windows. Therefore, this design eliminates the I/O-intensive and time-consuming step of additionally cropping large FoV regions from WSIs in previous studies. Moreover, since the ROI patch and its surrounding patches have the same magnification, we employ a shared image encoder to process both. To optimize memory efficiency during training, the numerous surrounding patches undergo feature extraction in a gradient-free manner, with weak augmentation applied to enrich data diversity while preserving the representation fidelity. Thereafter, we apply self-attention to integrate contextual information from individual surrounding patches, and then inject the consolidated features into the ROI patch’s embedding via cross-attention. Notably, to reduce the high computational overhead of attention operations, we propose a grid pooling technique to compress the dense feature maps of each surrounding patch into a few contextual tokens. The above designs collectively enable us to directly re-use the off-the-shelf features extracted from historically visited surrounding windows to perform context-aware nucleus detection, which further improves the inference efficiency. The most similar work to ours is [7], however, it focuses on tissue segmentation and overlooks the impact of pooling ratio and the benefits of weakly augmenting surrounding patches.

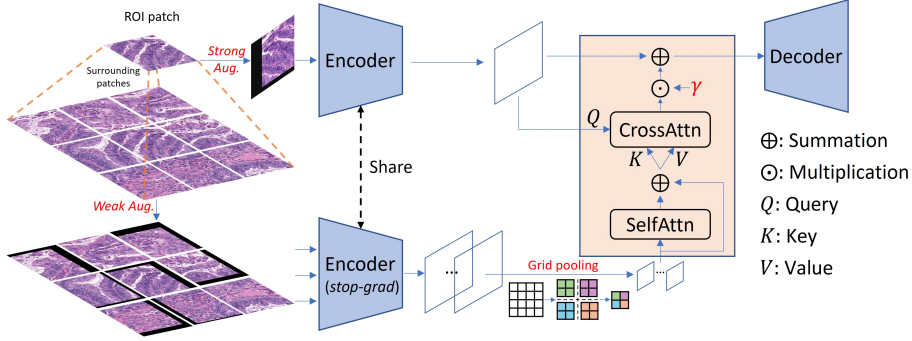


Fig. 3: Training details of our proposed context-aware nucleus detection method.

## 2 Method

### 2.1 Background

Typical nucleus detectors only takes a single patch as input. Such models are trained on an annotated patch set  $\mathcal{D}_l = \{(x_i, y_i)\}_{i=1}^N$ . For each patch  $x_i \in \mathbb{R}^{H \times W \times 3}$ , the annotation  $y_i$  comprises centroids and categories of all nuclei. To develop context-aware nucleus detector, each annotated patch  $x_i$  is complemented by its surrounding patches  $X_i = \{x_{i,j,k} \in \mathbb{R}^{H \times W \times 3} \mid j, k \in \{-\delta, \dots, \delta\}\}$ , where  $\delta$  denotes the size of context area perceived by the detector. For example, when  $\delta$  equals 1, the model learns to detect nuclei in the annotated patch while aggregating contextual information from a  $3 \times 3$  neighborhood comprising the annotated patch and its eight adjacent patches, as illustrated in Fig. 3.

### 2.2 Extraction of Contextual Information

Previous context-aware nucleus detection studies [1,2,23,20] all utilize additional large FoV patches to construct contextual information. Due to the inherent trade-off between learning global tissue context from large FoV patches and capturing local nuclear morphology in small FoV ones, these approaches adopt separate image encoders to process these two types of patches respectively.

In this work, we employ a shared image encoder to encode an annotated patch  $x_i$  into  $\mathcal{F}_i \in \mathbb{R}^{h \times w \times d}$  and its surrounding patches  $X_i$  into  $\mathcal{F}_{i,j,k} \in \mathbb{R}^{h \times w \times d}$ . Notably, the surrounding patches undergo feature extraction in a gradient-free mode. This design proves effective since the surrounding patches share the same magnification (*i.e.*, data distribution) as the annotated patch, thus allowing the encoder to parse them well without parameter adaptation. Moreover, this approach greatly saves training memory and allows the model to accommodate substantial contextual patches through memory overriding mechanism [18]. To build a comprehensive contextual representation, we flatten  $\{\mathcal{F}_{i,j,k} \mid j, k \in \{-\delta, \dots, \delta\}\}$  into 1D sequence  $\mathcal{S}_{ctx} \in \mathbb{R}^{(2\delta+1)^2 hw \times d}$  and apply self-attention to

facilitate inter-patch communication:

$$\mathcal{S}'_{ctx} = \mathcal{S}_{ctx} + \text{softmax} \left( \frac{(W_1^q \mathcal{S}_{ctx}) (W_1^k \mathcal{S}_{ctx})^T}{\sqrt{d}} \right) (W_1^v \mathcal{S}_{ctx}) \quad (1)$$

where  $W_1^q, W_1^k, W_1^v \in \mathbb{R}^{d \times d}$  are learnable weight matrices, residual connection is employed to stabilize training and preserve original features. However, we observe marginal improvements when all feature points of  $\mathcal{F}_{i,j,k}$  are utilized. This can be attributed to the redundancy in the high-level feature maps [15], as the feature points have already undergone sufficient information exchange through numerous convolutions (with kernel size larger than  $1 \times 1$ ) and pooling operations. This redundancy may impede the model in capturing discriminative contextual features, potentially resulting in sub-optimal performance. To deal with this, we partition  $\mathcal{F}_{i,j,k}$  into a uniform  $s \times s$  grid and apply average pooling within each grid cell, as illustrated by Fig. 3. We empirically set  $s \ll \min(h, w)$ , which not only diminishes the redundancy but also alleviates the computational overhead of self-attention by reducing the length of  $\mathcal{S}_{ctx}$  from  $(2\delta + 1)^2 hw$  to  $(2\delta + 1)^2 s^2$ .

### 2.3 Injection of Contextual Features

To enable context-aware nucleus detection, we inject the integrated contextual features  $\mathcal{S}'_{ctx}$  into the feature map  $\mathcal{F}_i$  extracted from the annotated patch. Specifically, we first flatten  $\mathcal{F}_i$  into a sequence  $\mathcal{S}_{tgt} \in \mathbb{R}^{hw \times d}$  and then use it to query relevant contextual information from  $\mathcal{S}'_{ctx}$  via cross-attention:

$$\mathcal{S}'_{tgt} = \mathcal{S}_{tgt} + \gamma * \text{softmax} \left( \frac{(W_2^q \mathcal{S}_{tgt}) (W_2^k \mathcal{S}'_{ctx})^T}{\sqrt{d}} \right) (W_2^v \mathcal{S}'_{ctx}) \quad (2)$$

where  $\gamma$  is a free paramter that explicitly modulates the weight of contextual features. Finally, the context-enriched  $\mathcal{S}'_{tgt}$  is fed into the decoder to predict nucleus centroids and categories. Notably, we observe no performance gains when incorporating positional embeddings in Eq. 1 and Eq. 2. We hypothesize that this is because histopathology slides are inherently continuous, where adjacent patches present coherent visual content along their boundaries, and this natural continuity implicitly encodes relative positional relationship.

### 2.4 Improving Model Performance via Weakly Perturbing Surrounding Patches

Data augmentation is one of the most powerful approaches to enhance the performance of deep neural networks [3,24,16]. As training context-free nucleus detectors [12], we apply strong augmentation including both photometric (*e.g.*, color jitter) and geometric (*e.g.*, random flipping) transformations for annotated patches. In this work, we further explore how can we augment the surrounding

patches for better performance. As these patches are encoded in a gradient-free manner, excessive augmentations can lead to out-of-distribution (OOD) representations [26] and consequently degrade model performance. We experimentally discover that random shifting and scaling of mild strength yields superior improvements. This effectiveness could be attributed to their capacity to eliminate redundant boundary information between adjacent patches, thereby enabling the model to better focus on informative contextual regions. Furthermore, to preserve relative positional information, we randomly apply this augmentation strategy with a moderate probability of 0.5 for each surrounding patch.

### 3 Results

#### 3.1 Experimental Settings

**Datasets.** The experimental evaluation is conducted on the publicly available OCELOT [20] dataset. Please refer to [20] for more details about this dataset. Moreover, we release OCELOT-seg in this work, the first benchmark dedicated to context-aware nucleus instance segmentation. To construct this dataset, we leverage PromptNucSeg-L [22], pre-trained on the large-scale PanNuke dataset [8,9], to generate instance masks from the point annotations in OCELOT. Then the masks are manually refined by two non-pathology PhD students under the guidance of a senior pathologist with over ten years of clinical expertise.

**Evaluation metrics.** For nucleus detection, we employ precision (P), recall (R) and F1-score as the evaluation metrics, which are calculated as in [20]. For nucleus instance segmentation, we adopt Panoptic Quality (PQ) as the primary evaluation metric, which can be decomposed into Detection Quality (DQ) and Segmentation Quality (SQ). Following [20], we repeat all experiments for 5 times and report the mean and 95% confidence interval of the performance metrics.

**Implementation details.** We adopt P2PNet [25] as the base nucleus detector. ResNet-50 [11] pre-trained on ImageNet-1K is used as the image encoder. Models are trained using the AdamW optimizer with learning rate of  $1e-4$  for 5 warm-up epochs and a total of 200 epochs. We use a batch size of 16, with all data distributed across 4 NVIDIA A100 GPUs.

#### 3.2 Comparison with the State-of-the-art Methods

Tab. 1 and Tab. 2 exhibit the performance comparison results on the detection and segmentation tasks, respectively. In case of nucleus detection, when  $\delta = 1$ , the proposed method surpasses the state-of-the-art (SOTA) counterpart MFoV-P2PNet by 1.57 points on average F1-score and the baseline P2PNet model by 3.75 points. When  $\delta = 2$ , our method outperforms SOTA by 1.66 points and the baseline approach by 4 points. In task of nucleus instance segmentation, when PromptNucSeg-B is used, our method achieves 1.89 and 2.91 points improvement over the SOTA and baseline models on average PQ score. And with PromptNucSeg-L, our method surpasses them by 1.92 and 2.96 points.

Table 1: Comparison of nucleus detection performance on the OCELOT benchmark. CA indicates a context-aware nucleus detector, and  $\delta$  represents the context region size. P2PNet serves as the baseline.

Method	CA	Background nucleus			Tumor nucleus			Average		
		P	R	F1	P	R	F1	P	R	F1
U-Net [19]		-	-	-	-	-	-	-	-	63.46 $\pm$ 4.59
DeepLabV3+ [5]		-	-	-	-	-	-	-	-	64.44 $\pm$ 1.82
Conditional DETR [17]	$\times$	66.91 $\pm$ 0.58	54.50 $\pm$ 1.52	60.02 $\pm$ 0.95	65.63 $\pm$ 1.32	79.02 $\pm$ 0.91	71.64 $\pm$ 0.50	66.27 $\pm$ 0.74	66.76 $\pm$ 0.42	65.83 $\pm$ 0.71
Deformable DETR [28]		66.76 $\pm$ 0.95	53.51 $\pm$ 1.18	59.34 $\pm$ 0.59	67.44 $\pm$ 0.87	75.82 $\pm$ 0.92	71.35 $\pm$ 0.40	67.10 $\pm$ 0.71	64.66 $\pm$ 0.17	65.34 $\pm$ 0.36
P2PNet [25]		66.03 $\pm$ 0.51	57.80 $\pm$ 0.25	61.64 $\pm$ 0.21	68.86 $\pm$ 0.20	76.66 $\pm$ 0.48	72.55 $\pm$ 0.27	67.44 $\pm$ 0.30	67.23 $\pm$ 0.21	67.09 $\pm$ 0.23
MFoVCE-Net [1]		-	-	-	-	-	-	-	-	67.12 $\pm$ 1.96
MFoV-P2PNet [23]	$\checkmark$	67.59 $\pm$ 0.15	60.61 $\pm$ 0.58	63.90 $\pm$ 0.28	70.57 $\pm$ 0.34	79.22 $\pm$ 0.15	74.64 $\pm$ 0.16	69.08 $\pm$ 0.12	69.91 $\pm$ 0.28	69.27 $\pm$ 0.22
E <sup>2</sup> -P2PNet (Ours)	( $\delta=1$ )	68.87 $\pm$ 0.41	64.18 $\pm$ 0.41	66.43 $\pm$ 0.10	72.67 $\pm$ 0.22	78.02 $\pm$ 0.72	75.24 $\pm$ 0.28	70.77 $\pm$ 0.15	71.10 $\pm$ 0.19	70.84 $\pm$ 0.15
$\Delta_{baseline}$		-	-	+4.79	-	-	+2.69	-	-	+3.75
$\Delta_{sota}$		-	-	+2.53	-	-	+0.60	-	-	+1.57
MFoV-P2PNet [23]	$\checkmark$	67.85 $\pm$ 0.15	60.95 $\pm$ 1.28	64.18 $\pm$ 0.71	70.68 $\pm$ 0.63	79.17 $\pm$ 0.25	74.67 $\pm$ 0.35	69.26 $\pm$ 0.34	70.06 $\pm$ 0.6	69.43 $\pm$ 0.52
E <sup>2</sup> -P2PNet (Ours)	( $\delta=2$ )	68.41 $\pm$ 0.34	65.27 $\pm$ 0.98	66.80 $\pm$ 0.64	73.24 $\pm$ 0.8	77.69 $\pm$ 0.31	75.38 $\pm$ 0.31	70.82 $\pm$ 0.54	71.48 $\pm$ 0.38	71.09 $\pm$ 0.48
$\Delta_{baseline}$		-	-	+5.16	-	-	+2.83	-	-	+4.00
$\Delta_{sota}$		-	-	+2.62	-	-	+0.71	-	-	+1.66

Table 2: Comparison of nucleus instance segmentation performance on our crafted OCELOT-seg benchmark. Due to page limitations, we only report the results at  $\delta = 1$ .

Framework	Method	CA	Background nucleus			Tumor nucleus			Average		
			DQ	SQ	PQ	DQ	SQ	PQ	DQ	SQ	PQ
-	Hover-Net [10]	$\times$	48.14 $\pm$ 0.70	87.11 $\pm$ 0.10	43.44 $\pm$ 0.63	67.65 $\pm$ 0.38	88.10 $\pm$ 0.11	61.15 $\pm$ 0.40	57.89 $\pm$ 0.31	87.60 $\pm$ 0.10	52.29 $\pm$ 0.29
PromptNucSeg-B	Conditional DETR	$\times$	47.97 $\pm$ 0.84	86.95 $\pm$ 0.53	43.94 $\pm$ 0.83	71.44 $\pm$ 0.61	88.90 $\pm$ 0.83	65.54 $\pm$ 0.55	59.70 $\pm$ 0.60	87.93 $\pm$ 0.46	54.74 $\pm$ 0.57
	Deformable DETR	$\times$	46.99 $\pm$ 0.50	86.39 $\pm$ 0.86	43.08 $\pm$ 0.51	70.93 $\pm$ 0.63	90.22 $\pm$ 0.24	65.09 $\pm$ 0.60	58.96 $\pm$ 0.30	88.30 $\pm$ 0.50	54.09 $\pm$ 0.30
	P2PNet	$\times$	48.31 $\pm$ 0.38	88.35 $\pm$ 0.47	44.44 $\pm$ 0.36	72.14 $\pm$ 0.31	91.08 $\pm$ 0.24	66.21 $\pm$ 0.28	60.22 $\pm$ 0.30	89.71 $\pm$ 0.28	55.33 $\pm$ 0.28
	MFoV-P2PNet	$\checkmark$	49.55 $\pm$ 0.20	86.69 $\pm$ 0.45	45.52 $\pm$ 0.16	73.21 $\pm$ 0.30	90.70 $\pm$ 0.02	67.18 $\pm$ 0.29	61.38 $\pm$ 0.15	88.70 $\pm$ 0.23	56.35 $\pm$ 0.15
	E <sup>2</sup> -P2PNet (Ours)	$\checkmark$	53.20 $\pm$ 0.40	87.83 $\pm$ 0.47	48.85 $\pm$ 0.36	73.62 $\pm$ 0.32	90.72 $\pm$ 0.30	67.62 $\pm$ 0.29	63.41 $\pm$ 0.32	89.27 $\pm$ 0.29	58.24 $\pm$ 0.29
	$\Delta_{baseline}$		-	-	+4.41	-	-	+1.41	-	-	+2.91
PromptNucSeg-L	Conditional DETR	$\times$	48.01 $\pm$ 0.84	86.91 $\pm$ 0.49	43.97 $\pm$ 0.82	71.58 $\pm$ 0.61	88.91 $\pm$ 0.82	65.68 $\pm$ 0.55	59.79 $\pm$ 0.59	87.91 $\pm$ 0.45	54.83 $\pm$ 0.57
	Deformable DETR	$\times$	46.95 $\pm$ 0.50	86.47 $\pm$ 0.84	43.08 $\pm$ 0.49	71.06 $\pm$ 0.63	90.12 $\pm$ 0.27	65.24 $\pm$ 0.60	59.01 $\pm$ 0.30	88.29 $\pm$ 0.50	54.16 $\pm$ 0.30
	P2PNet	$\times$	48.34 $\pm$ 0.37	88.36 $\pm$ 0.48	44.47 $\pm$ 0.36	72.25 $\pm$ 0.29	91.10 $\pm$ 0.24	66.34 $\pm$ 0.28	60.29 $\pm$ 0.27	89.73 $\pm$ 0.29	55.41 $\pm$ 0.26
	MFoV-P2PNet	$\checkmark$	49.60 $\pm$ 0.17	86.82 $\pm$ 0.43	45.59 $\pm$ 0.15	73.30 $\pm$ 0.31	90.72 $\pm$ 0.03	67.29 $\pm$ 0.30	61.45 $\pm$ 0.15	88.77 $\pm$ 0.23	56.44 $\pm$ 0.15
	E <sup>2</sup> -P2PNet (Ours)	$\checkmark$	53.21 $\pm$ 0.39	87.99 $\pm$ 0.46	48.95 $\pm$ 0.36	73.75 $\pm$ 0.34	90.71 $\pm$ 0.31	67.77 $\pm$ 0.31	63.48 $\pm$ 0.32	89.35 $\pm$ 0.28	58.36 $\pm$ 0.30
	$\Delta_{baseline}$		-	-	+4.48	-	-	+1.43	-	-	+2.95
	$\Delta_{sota}$		-	-	+3.36	-	-	+0.48	-	-	+1.92

Tab. 3 presents a comprehensive comparison of model size, computational cost, and inference efficiency across different methods. All metrics were measured on a system with a single NVIDIA A100 GPU and an Intel Xeon Platinum 8358 CPU (2.60GHz, 64 cores, 128 threads). Compared to the baseline context-free nucleus detector, our method introduces minimal computational overhead while achieving significant performance improvements (see Tab. 1 and Tab. 2). Notably, the proposed model runs 3.26 $\times$  faster than the SOTA method.

## 4 Ablation study

We evaluate the efficacy of our proposed modules at  $\delta = 1$ . **Effect of  $s$ .** Fig. 5 exhibits the impact of pooling grid number on model performance. Intuitively, increasing the grid number results in finer-grained partitioning, thereby preserving more comprehensive contextual details and leading to improved performance. However, due to the redundancy among high-level feature points [15], overly fine



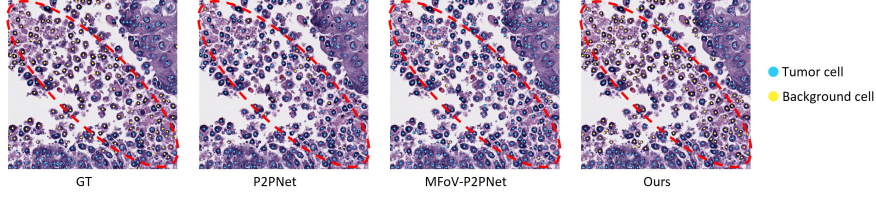


Fig. 4: Qualitative comparison results.

Table 3: Comparison on model size, computational cost and efficiency of different methods. The inference time is measured using a WSI with approximately 3k foreground sliding windows of size  $1024 \times 1024$ .

Method	Params (M)	Time (s)	FLOPs (G)
P2PNet	27.26	98.04	100.08
MFoV-P2PNet	53.22	356.87	212.75
E <sup>2</sup> -P2PNet (Ours)	60.79	109.98	115.92

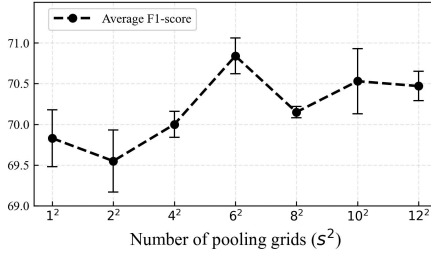


Fig. 5: Effect of pooling grid number.

Table 4: Effect of weight item  $\gamma$ .

$\gamma$	1	2	3
F1-score	$70.71 \pm 0.18$	$70.84 \pm 0.15$	$69.48 \pm 0.32$

Table 5: Effect of applying weak augmentation on surrounding patches.

Aug.	-	Weak	Strong
F1-score	$70.37 \pm 0.25$	$70.84 \pm 0.15$	$69.88 \pm 0.33$

partitioning may hinder the model from capturing discriminative contextual features and result in sub-optimal performance. Consequently, the best performance is observed when  $s = 6$ . **Effect of  $\gamma$ .** In Tab. 4, we explore the effect of weight item  $\gamma$  that explicitly modulates the model’s attention to contextual features. It can be observed that  $\gamma = 2$  yields slightly better performance compared to  $\gamma = 1$ . Nevertheless, further increasing  $\gamma$  causes the model to neglect critical nuclear morphological features and results in performance degradation. **Effect of weakly perturbing surrounding patches.** In Tab. 5, we ablate the effect of various augmentation techniques applied to surrounding patches. We discover that applying strong augmentations leads to significant performance degradation. As these surrounding patches are encoded in gradient-free mode, strong augmentations can produce OOD representations that confuse the model. In contrast, employing weak augmentation (*i.e.*, random shifting and scaling here) yields remarkable performance improvements. We implement this augmentation



strategy using the ShiftScaleRotate class from the Albumentations library [4] with hyper-parameters `shift_limit=0.2` and `scale_limit=0.1`.

## 5 Conclusion

In this paper, we propose an effective and efficient context-aware nucleus detection approach. Instead of using additional large FoV patches in previous methods, we aggregate contextual information from historically visited sliding windows during whole-slide inference, which greatly improves the inference speed. Besides, compared to large FoV patches, the sliding patches have higher magnification and provide finer-grained context details, which lead to better detection outcomes. Extensive experiments demonstrate the superiority of our method.

**Acknowledgments.** This study was partially supported by Zhejiang Provincial Natural Science Foundation of China (Grant No.XHD23F0201), the National Natural Science Foundation of China (Grant No.92270108), foundation of Muyuan Laboratory (Program ID: 14106022401,14106022402), the Research Center for Industries of the Future (RCIF) at Westlake University, and the Westlake Education Foundation.

## References

1. Bai, T., Xu, J., Xing, F.: Multi-field of view aggregation and context encoding for single-stage nucleus recognition. In: Medical Image Computing and Computer Assisted Intervention–MICCAI 2020: 23rd International Conference, Lima, Peru, October 4–8, 2020, Proceedings, Part V 23. pp. 382–392. Springer (2020)
2. Bai, T., Xu, J., Zhang, Z., Guo, S., Luo, X.: Context-aware learning for cancer cell nucleus recognition in pathology images. *Bioinformatics* **38**(10), 2892–2898 (2022)
3. Bai, Y., Chen, D., Li, Q., Shen, W., Wang, Y.: Bidirectional copy-paste for semi-supervised medical image segmentation. In: Proceedings of the IEEE/CVF conference on computer vision and pattern recognition. pp. 11514–11524 (2023)
4. Buslaev, A., Iglovikov, V.I., Khvedchenya, E., Parinov, A., Druzhinin, M., Kalinin, A.A.: Albumentations: Fast and flexible image augmentations. *Information* **11**(2) (2020). <https://doi.org/10.3390/info11020125>, <https://www.mdpi.com/2078-2489/11/2/125>
5. Chen, L.C., Zhu, Y., Papandreou, G., Schroff, F., Adam, H.: Encoder-decoder with atrous separable convolution for semantic image segmentation. In: Proceedings of the European conference on computer vision (ECCV). pp. 801–818 (2018)
6. Diao, J.A., Wang, J.K., Chui, W.F., Mountain, V., Gullapally, S.C., Srinivasan, R., Mitchell, R.N., Glass, B., Hoffman, S., Rao, S.K., et al.: Human-interpretable image features derived from densely mapped cancer pathology slides predict diverse molecular phenotypes. *Nature communications* **12**(1), 1613 (2021)
7. Ester, O., Hörst, F., Seibold, C., Keyl, J., Ting, S., Vasileiadis, N., Schmitz, J., Ivanyi, P., Grünwald, V., Bräsen, J.H., et al.: Valuing vicinity: Memory attention framework for context-based semantic segmentation in histopathology. *Computerized Medical Imaging and Graphics* **107**, 102238 (2023)
8. Gamper, J., Koohbanani, N.A., Benes, K., Khuram, A., Rajpoot, N.: Pannuke: an open pan-cancer histology dataset for nuclei instance segmentation and classification. In: European Congress on Digital Pathology. pp. 11–19. Springer (2019)

9. Gamper, J., Koohbanani, N.A., Graham, S., Jahanifar, M., Khurram, S.A., Azam, A., Hewitt, K., Rajpoot, N.: Pannuke dataset extension, insights and baselines. arXiv preprint arXiv:2003.10778 (2020)
10. Graham, S., Vu, Q.D., Raza, S.E.A., Azam, A., Tsang, Y.W., Kwak, J.T., Rajpoot, N.: Hover-net: Simultaneous segmentation and classification of nuclei in multi-tissue histology images. *Medical image analysis* **58**, 101563 (2019)
11. He, K., Zhang, X., Ren, S., Sun, J.: Deep residual learning for image recognition. In: *Proceedings of the IEEE conference on computer vision and pattern recognition*. pp. 770–778 (2016)
12. Hörst, F., Rempe, M., Heine, L., Seibold, C., Keyl, J., Baldini, G., Ugurel, S., Siveke, J., Grünwald, B., Egger, J., et al.: Cellvit: Vision transformers for precise cell segmentation and classification. *Medical Image Analysis* **94**, 103143 (2024)
13. Huang, J., Li, H., Wan, X., Li, G.: Affine-consistent transformer for multi-class cell nuclei detection. In: *Proceedings of the IEEE/CVF International Conference on Computer Vision*. pp. 21384–21393 (2023)
14. Huang, Z., Ding, Y., Song, G., Wang, L., Geng, R., He, H., Du, S., Liu, X., Tian, Y., Liang, Y., et al.: Bcdata: A large-scale dataset and benchmark for cell detection and counting. In: *Medical Image Computing and Computer Assisted Intervention–MICCAI 2020: 23rd International Conference, Lima, Peru, October 4–8, 2020, Proceedings, Part V* 23. pp. 289–298. Springer (2020)
15. Li, J., Wen, Y., He, L.: Seconv: Spatial and channel reconstruction convolution for feature redundancy. In: *Proceedings of the IEEE/CVF Conference on Computer Vision and Pattern Recognition*. pp. 6153–6162 (2023)
16. Liu, Y.C., Ma, C.Y., He, Z., Kuo, C.W., Chen, K., Zhang, P., Wu, B., Kira, Z., Vajda, P.: Unbiased teacher for semi-supervised object detection. arXiv preprint arXiv:2102.09480 (2021)
17. Meng, D., Chen, X., Fan, Z., Zeng, G., Li, H., Yuan, Y., Sun, L., Wang, J.: Conditional detr for fast training convergence. In: *Proceedings of the IEEE/CVF international conference on computer vision*. pp. 3651–3660 (2021)
18. Paszke, A., Gross, S., Massa, F., Lerer, A., Bradbury, J., Chanan, G., Killeen, T., Lin, Z., Gimelshein, N., Antiga, L., et al.: Pytorch: An imperative style, high-performance deep learning library. *Advances in neural information processing systems* **32** (2019)
19. Ronneberger, O., Fischer, P., Brox, T.: U-net: Convolutional networks for biomedical image segmentation. In: *Medical image computing and computer-assisted intervention–MICCAI 2015: 18th international conference, Munich, Germany, October 5–9, 2015, proceedings, part III* 18. pp. 234–241. Springer (2015)
20. Ryu, J., Puche, A.V., Shin, J., Park, S., Brattoli, B., Lee, J., Jung, W., Cho, S.I., Paeng, K., Ock, C.Y., et al.: Ocelot: Overlapped cell on tissue dataset for histopathology. In: *Proceedings of the IEEE/CVF Conference on Computer Vision and Pattern Recognition*. pp. 23902–23912 (2023)
21. Shui, Z., Zhang, S., Zhu, C., Wang, B., Chen, P., Zheng, S., Yang, L.: End-to-end cell recognition by point annotation. In: *International Conference on Medical Image Computing and Computer-Assisted Intervention*. pp. 109–118. Springer (2022)
22. Shui, Z., Zhang, Y., Yao, K., Zhu, C., Zheng, S., Li, J., Li, H., Sun, Y., Guo, R., Yang, L.: Unleashing the power of prompt-driven nucleus instance segmentation. In: *European Conference on Computer Vision*. pp. 288–304. Springer (2024)
23. Shui, Z., Zheng, S., Zhu, C., Zhang, S., Yu, X., Li, H., Li, J., Chen, P., Yang, L.: Dpa-p2pnet: deformable proposal-aware p2pnet for accurate point-based cell detection. In: *Proceedings of the AAAI Conference on Artificial Intelligence*. vol. 38, pp. 4864–4872 (2024)

24. Sohn, K., Berthelot, D., Carlini, N., Zhang, Z., Zhang, H., Raffel, C.A., Cubuk, E.D., Kurakin, A., Li, C.L.: Fixmatch: Simplifying semi-supervised learning with consistency and confidence. *Advances in neural information processing systems* **33**, 596–608 (2020)
25. Song, Q., Wang, C., Jiang, Z., Wang, Y., Tai, Y., Wang, C., Li, J., Huang, F., Wu, Y.: Rethinking counting and localization in crowds: A purely point-based framework. In: *Proceedings of the IEEE/CVF International Conference on Computer Vision*. pp. 3365–3374 (2021)
26. Wang, Y., Qiao, P., Liu, C., Song, G., Zheng, X., Chen, J.: Out-of-distributed semantic pruning for robust semi-supervised learning. In: *Proceedings of the IEEE/CVF Conference on Computer Vision and Pattern Recognition*. pp. 23849–23858 (2023)
27. Zhang, S., Zhu, C., Li, H., Cai, J., Yang, L.: Weakly supervised learning for cell recognition in immunohistochemical cytoplasm staining images. In: *2022 IEEE 19th International Symposium on Biomedical Imaging (ISBI)*. pp. 1–5. IEEE (2022)
28. Zhu, X., Su, W., Lu, L., Li, B., Wang, X., Dai, J.: Deformable detr: Deformable transformers for end-to-end object detection. *arXiv preprint arXiv:2010.04159* (2020)